Journal Pre-proof

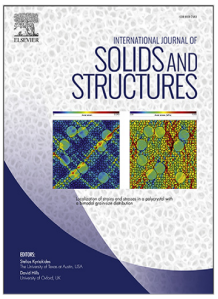

Mass efficiency of strip-based coilable space structures

Andrew J. Lee, Sergio Pellegrino

PII: S0020-7683(22)00335-3
DOI: https://doi.org/10.1016/j.ijsolstr.2022.111867
Reference: SAS 111867

To appear in: *International Journal of Solids and Structures*

Received date : 21 October 2021
Revised date : 21 June 2022
Accepted date : 12 July 2022

Please cite this article as: A.J. Lee and S. Pellegrino, Mass efficiency of strip-based coilable space structures. *International Journal of Solids and Structures* (2022), doi: https://doi.org/10.1016/j.ijsolstr.2022.111867.

Mass Efficiency of Strip-Based Coilable Space Structures

Andrew J. Lee[1], Sergio Pellegrino*

Graduate Aerospace Laboratories, California Institute of Technology
Pasadena, CA 91125, USA

Abstract

This paper presents a general semi-analytical study of the mass efficiency of coilable plate-like space structures. A bending architecture based on four diagonal booms that support parallel strips is compared to a cable-stayed architecture in which vertical booms and cable stays support the diagonal booms at the tip. Limiting conditions of global buckling, local buckling, material failure, and excessive deflection define the design space for each architecture. Considering pressure loads spanning several orders of magnitude, the optimal areal density of structures of size varying from a few meters to hundreds of meters is determined for both architectures. Design charts for optimal designs are provided for a range of sizes, loads, and deflection limits. It is shown that the cable-stayed architecture is always lighter than the bending architecture, from a few percent to over 30%.

Keywords: Space structures, structural design, mass efficiency, areal density, deployable, cable-stayed

*Corresponding author
Email address: sergiop@caltech.edu (Sergio Pellegrino)
URL: http://www.pellegrino.caltech.edu/ (Sergio Pellegrino)
[1]Currently at: Department of Mechanical and Aerospace Engineering, NC State University, Raleigh, NC 27695

Nomenclature

EI	Flexural stiffness
H	Height of vertical booms
$\hat{H}$	Normalized height
L	Side length of structure (span)
M	Max. bending moment
m_b	Mass of booms
n	Number of strips per quadrant
P	Pressure
r	Boom radius
R	Longeron radius
$t,\ t_f$	Boom wall thickness, longeron flange thickness
w_j	Max. cable sag
w_s	Max. strip deflection
w_n	Boom tip deflection
w	Total max. deflection
ϵ_f	Failure strain
$\rho_{b,cs}$	Areal density of booms and cables
ρ_s	Areal density of strips
ρ^{total}	Total areal density
θ	Longeron subtended angle

Subscripts

$[\ ]_b$	Bending architecture or boom
$[\ ]_{cs}$	Cable-stayed architecture
$[\ ]_i$	ith strip of quadrant
$[\ ]_s$	Strip

Superscripts

$[\ ]^d$	Excessive deflection or diagonal boom
$[\ ]^g$	Global buckling
$[\ ]^f$	Material failure
$[\ ]^l$	Local shell buckling
$[\ ]^{lim}$	Design limit
$[\ ]^v$	Vertical boom

1. Introduction

Deployable space structures are required to be extremely lightweight and packageable into small volumes. These objectives can be pursued through different structural concepts and architectures.

Exquisite solutions to this problem have been developed for many specific applications (Miura and Pellegrino, 2020) and their superiority has typically been demonstrated by showing higher mass efficiency over an expected range of scales, loading environments, etc. However, there has been a lack of broader studies providing general trade-offs between different structural architectures across a wide range of scales and environments, which limits the potential for significant advances in future space exploration.

Recent advances in structural materials and manufacturing technologies have broadened the range of practically feasible structural architectures. Coupled with space exploration mission concepts with unprecedented requirements, currently on the horizon, the potential importance of such broader studies has greatly increased.

For a practical impact, it is important to focus these studies on advanced architectures that are at the cutting edge of achievable performance, although this increases the complexity of these studies. Advanced architectures combine different load-carrying modes, which have to be optimized with suitable analytical formulations. The present study shows a systematic way of doing this, considering two different architectures for coilable space structures that are currently under development for large solar arrays (KISS, 2022) and space solar power stations (Gdoutos et al., 2020).

The first architecture will be described as the bending architecture and is schematically shown in Fig. 1(a). It is a square structure of size $L \times L$, composed of long and narrow, parallel strips that can support photovoltaic and/or RF power radiation films. The strips are bending-stiff structures supported by four diagonal booms, also loaded in bending, through four diagonal cables. Each cable is connected to the central hub and to the tip of a boom. Bending of the

booms and strips is the main load-carrying mode for this structure when it is loaded by a transverse pressure, and the structure can be efficiently packaged through a combination of origami-inspired folding and coiling, schematically shown in Fig. 2 (Arya et al., 2016).

The second architecture considered in this paper, inspired by cable-stayed bridges (Fairclough et al., 2018) and large deployable space structures for solar reflectors (Hedgepeth, 1981) and antennas (Campbell, 1981; Belvin, 1984), uses cable stays to increase the stiffness of the diagonal booms. It will be described as the cable-stayed architecture. The specific architecture considered in this paper includes two vertical booms of length H connected by cable stays to the diagonal boom tips, Fig. 1(b). When a transverse pressure is applied to this structure, the top vertical boom and the four stays connected to it support the diagonal booms against downward deflection, while the bottom stays become slack. The bottom vertical boom and the stays connected to it support the diagonal booms when the direction of the pressure is reversed.

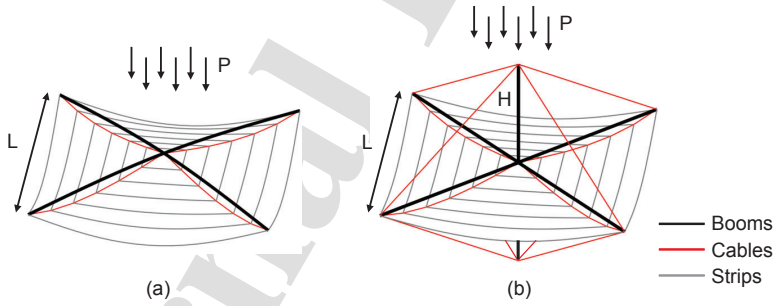

Figure 1: (a) Bending and (b) cable-stayed architectures for square space structure loaded by a pressure P. The side length is L and the height of the vertical boom for the cable-stayed architecture is H.

Comparing the performance of the bending and cable-stayed architectures is the goal of this paper. The objective of the present study is to quantify the mass reduction that can be achieved by introducing the cable stays, which decrease

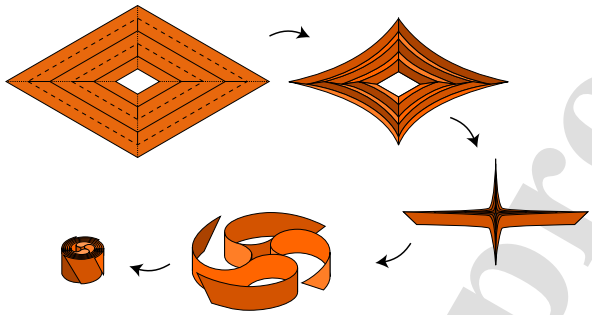

Figure 2: Schematic of packaging concept.

the bending deformation of the diagonal booms and thus increase the lateral stiffness of the structure, while taking into account the mass increase associated with the axial compression applied to the booms by the stays. To avoid buckling, these booms have to be made thicker and with a larger diameter. Specific questions arising are if the performance advantage for cable-stayed architectures will be general, or limited to a range of loads or structural spans, and how significant is the mass advantage. These questions will be addressed in the paper by comparing the areal densities of the lightest possible structures that can be designed with both architectures, for varying load magnitude and structural span.

A difference between the present paper and existing work is that previously only the scaling of the design parameters for a specific architecture has been considered. Heard et al. (1981) compared deployable vs. in-space erectable for plate-like trusses of two specific sizes and subject to a specific vibration frequency constraint. Greschik and Mikulas (2002) studied 100 m solar sails with a bending architecture and a specific film architecture. Banik and Maji (2016) considered tensioned blanket solar arrays with either one or two deployable booms.

The paper is organized as follows. Section 2 presents the overall approach, which consists in defining for each architecture a set of design parameters, and to

derive the pressure loads that correspond to buckling, material failure, and excessive compliance. Section 3 focuses on the strips that form the four quadrants in both architectures. Finite element simulations are combined with analytical expressions to predict the pressures that cause local shell buckling or excessive deflection of the strips. The strip design limits and the optimal areal density for a wide range of structural spans are derived. Sections 4 and 5 present the analytical formulations for obtaining the design limits for the booms and cables for the bending and cable-stayed architectures, respectively. Minimal mass designs for each architecture, including the strips, are then obtained. Section 7 compares the mass efficiency of the optimized architectures and identifies the superior architecture for a range of lengths and loads. It also presents and compares optimal designs based on both architectures, for a specific example. Section 8 concludes the paper.

2. Approach

An integrated design approach was adopted, setting identical metrics, limits, and parameter spaces between different architectures. Concurrent optimization of major structural elements then occurs within these constraints. This approach allows the peak performance of each architecture to be compared against one another without bias due to differing design conditions.

This approach was inspired by a paper on compression structures by Budiansky (1999), which compared the mass efficiency of different types of columns. Budiansky compared columns with solid square or circular cross-sections, to columns based on metal-foam-filled tubes, to tubes whose walls are foam-core sandwiches, and also to tubes made from panels with hat stiffeners. Budiansky derived a common set of structural indices applicable to each type of cross-section. These indices were based on the column's geometry, material properties, and compressive strength. He then used these design parameters to minimize the weight, which were subsequently compared to ascertain the relative performance of each column type.

There are two similarities between the problem studied by Budiansky and the present one. First, each design is characterized by several parameters, making the overall design space very large and hence suggesting that the simultaneous "brute force" optimization of all design parameters would not be the best approach. Second, basic analytical or semi-analytical structural mechanics solutions are available for many of the quantities of interest, making it possible to derive inverse relationships that can be used to implicitly satisfy design conditions (inequalities), etc. A further benefit of adopting a semi-analytical approach is that, since we are interested in comparing solutions across a wide range of spans and loads, the detailed evaluation of many specific designs would not be feasible.

The design of the strips is considered first, since the strips are an element common to both architectures and their design is independent from the other load carrying elements. A mass efficient design is chosen for the strips, using coilable thin shells that form stiff, lightweight frames. Once the strips have been optimized, the design of the diagonal booms and cords for the bending architecture is considered. Then, the design of the diagonal booms and cords, and of the vertical booms for the cable-stayed architecture completes the initial part of the study. For each component type, its contribution to the areal density of the complete structure is derived and the sum of these contributions yields the overall areal density of each structure.

It is important to note that only the mass of the structural elements is included in the calculation of the areal densities. The mass of the deployment devices and the functional elements, such as the solar cells and the electrical blankets for a solar array, is not included.

Each design problem is formulated in terms of finding the maximum pressure that can be carried without reaching a specific type of failure (global buckling, local buckling or material failure) of that component, making reasonable assumptions for the buckling modes which, of course, would require a detailed verification at a later, detailed design stage. Additionally, a limit on the maximum acceptable compliance of the structure is set at a global level.

A uniform pressure P over the whole structure is the assumed external loading, with a six degree of freedom rigid-body constraint applied at the center of the structure. In reality, the structure would be part of a spacecraft system that operates under dynamic conditions, and the actual loads on the structure would result from solar pressure, gravity gradients and inertial forces due to station-keeping maneuvers. The magnitudes of these loads depends on the specific application. Inertial loads depend on the areal density of the structure as well as the design of the attitude control system of the spacecraft (Hedgepeth, 1981). For generality, it is assumed that all of these effects can be captured through an equivalent static pressure.

Table 1 presents the notation that is used for the values of the pressure P that correspond to each specific mode of failure. Note that the subscripts b, cs, and s denote the bending architecture, the cable-stayed architecture, and the strips, respectively. Also, the superscripts g, l, f, and d for the bending architecture denote global buckling, local shell buckling, material failure, and excessive deflection, respectively. For the cable-stayed architecture, the superscripts g, l, f denote global buckling, local shell buckling, and material failure, respectively, and d and v denote the diagonal and vertical booms, respectively. Material failure of the strips due to pressure is not considered, as the buckling or deflection limits are always reached first.

Table 1: Pressure values corresponding to each design limit.

	Strips	Bending: Boom	Cable-stayed: Vertical Boom	Cable-stayed: Diagonal Boom
Global Buckling	N/A	P_b^g	$P_{cs}^{v,g}$	$P_{cs}^{d,g}$
Local Buckling	P_s^l	P_b^l	$P_{cs}^{v,l}$	$P_{cs}^{d,l}$
Material Failure	N/A	P_b^f	$P_{cs}^{v,f}$	$P_{cs}^{d,f}$
Deflection	P_s^d	P_b^d	N/A	N/A

The flowchart in Fig. 3 outlines the procedure for obtaining the minimum areal densities of both architectures for mass efficiency comparisons.

It should be noted that the structures considered in this study are four-fold symmetric around a vertical axis and they also have four vertical planes of mirror symmetry. Hence their analysis has been simplified by exploiting symmetry considerations.

3. Design Limits for the Strips

The strips are arranged to form four identical quadrants, with n strips of equal width, W, in each quadrant, as shown in Fig. 4. The innermost strip has length $L_1 = \sqrt{2}W$ and the outermost strip has length $L_n = n\sqrt{2}W = L$. To form a gap-free surface, the strips need to be of trapezoidal shape (Gdoutos et al., 2020) but in the present analysis their shape is simplified to a rectangle, as shown in Fig. 4. With this assumption, the pressure loading is mirror-symmetric with respect to the center line of each rectangle.

To achieve a high stiffness-to-mass ratio, a strip architecture with edge longerons that can be elastically flattened and coiled was chosen. A ladder-type structure consisting of two Triangular Rollable and Collapsible (TRAC) longerons (Murphey and Banik, 2011; Royer and Pellegrino, 2020) transversely connected by regularly spaced battens is particularly well suited for the present application. The longerons are thin composite shells consisting of two flanges connected to a web, Fig. 5, and the battens are rods with a rectangular cross-section. More details are provided in Appendix A.

It is shown in Appendix B that for the chosen longerons the strip buckling moment varies with the angle θ according to Fig. B.22. Hence, the strip buckling pressure can be obtained from:

$$P_s^l = \frac{8M_s^l}{WL_i^2} \tag{1}$$

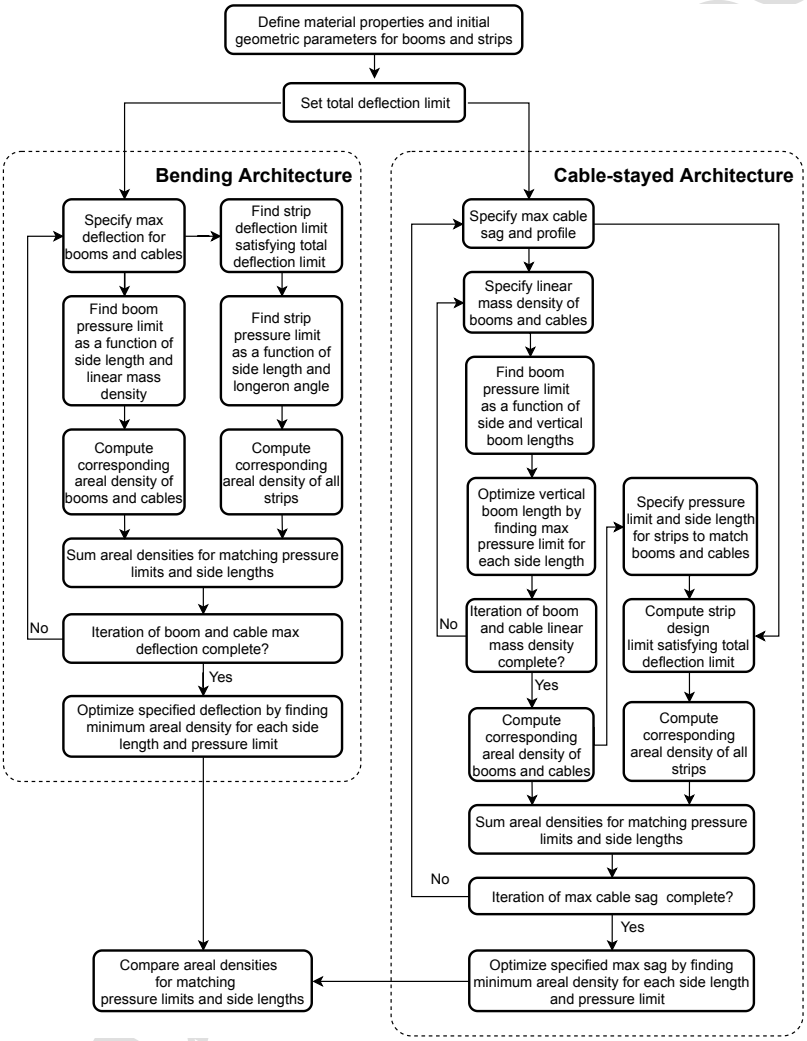

Figure 3: Procedure for obtaining optimal areal densities.

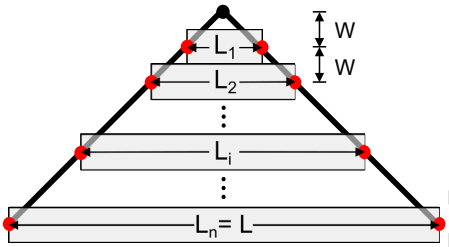

Figure 4: Definition of strip lengths and area allocated to each strip for loading analysis.

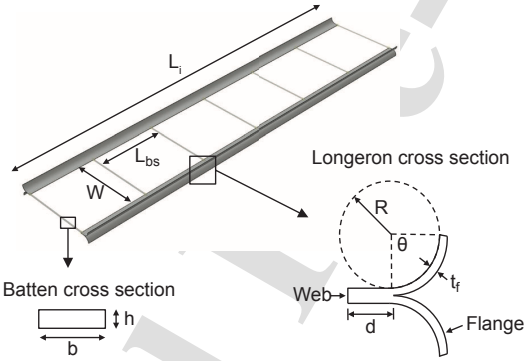

Figure 5: Schematic of ith strip consisting of longerons and battens.

3.1. Deflection Limit

The strips were modeled as simply supported beams of flexural stiffness EI_s equal to twice the stiffness of a longeron (Leclerc, 2020) and given by:

$$EI_s = 4\left(A_{11} - \frac{A_{12}^2}{A_{22}}\right)\left[d\bar{t}^2 + \frac{R^2}{2}\sin\theta\left(R\cos\theta - 4\left(R + \bar{t}\right)\right) + \frac{3R\theta}{2}\left(R^2 + \frac{4R\bar{t}}{3} + \frac{2\bar{t}^2}{3}\right)\right] \tag{2}$$

where $\bar{t} = \frac{1}{2}\left(t_f + t_{GFPW}\right)$ and A_{11}, A_{12}, and A_{22} are the in-plane extensional stiffness terms in Table A.3. Substituting the parameters defined in Appendix A, EI_s is only a function of the subtended angle θ.

The pressure corresponding to a given maximum deflection at mid-span, w_s, under a uniformly distributed loading $P_s^d W$, is given by:

$$P_s^d = \frac{384 E I_s w_s}{5 W L_i^4} \tag{3}$$

3.2. Design Limits

The pressure limit, P_s^{lim}, for a strip is found by considering the smallest among two pressure values. The third limit, material failure, has already been taken into account, by choosing a value of the flange radius that allows flattening and coiling of the strip, Eq. A.1. Therefore:

$$P_s^{lim} = \min\left\{P_s^l, P_s^d\right\} \tag{4}$$

Here it is noted that both values are lowest for the longest strip in the structure and hence $L_i = L$ is used to calculate these limits.

As an example, a deflection limit of $w_s = 0.1L$ for the outermost strip was considered. Figure 6 shows plots of P_s^{lim} as a function of L, for $\theta = 45°, 90°$, and $135°$. The smallest span considered is $L = 6$ m which corresponds to a structure with only three strips per quadrant. Designs limited by buckling are denoted with dashed lines, identifying strips that would buckle before reaching the specified deflection limit. In most of the design space the strip designs are deflection limited; buckling becomes dominant only for shorter spans and larger subtended angles. Note that the range of spans for which the strips are limited by buckling grows with increasing values of θ.

A more complete understanding of the contribution of the strips to the overall mass of the structure is provided by the areal density of strips that reach the performance limits. It is obtained from:

$$\rho_s = \frac{4}{L^2} \sum_{i=1}^{n} \left(2m_s^l + m_s^b\right)_i \tag{5}$$

where m_s^l, m_s^b are the mass of a single longeron and of all the battens, respectively, in the ith strip. They are given by:

$$\left(m_s^l\right)_i = L_i \left[2\left(R\theta + d\right)\left([n\rho t]_{CF} + [n\rho t]_{GFPW}\right) + d[\rho t]_{GFPW}\right] \tag{6}$$

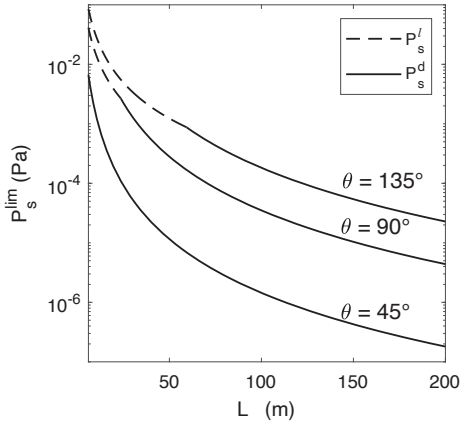

Figure 6: Strip pressure limit as a function of span for longeron subtended angles $\theta = 45°, 90°$, and 135°. The deflection limit is $w_s = 0.1L$.

$$\left(m_s^b\right)_i = \left\lfloor \frac{L_i}{L_{bs}} \right\rfloor \rho_{CF} b h L_b \tag{7}$$

In Eq. 6, n_{CF} and n_{GFPW} are respectively the number of unidirectional carbon fiber and glass fiber plain weave plies in the flange laminate. The lamina densities are $\rho_{CF} = 1200$ kg/m^3 and $\rho_{GFPW} = 1900$ kg/m^3. In Eq. 7, $\left\lfloor \frac{L_i}{L_{bs}} \right\rfloor$ is the number of battens in the ith strip.

The areal density of the strips has been plotted in Fig. 7, in terms of L and θ. Note that a red line separates the regions of the design space dominated by different pressure limits. An upper limit of $\theta = 180°$ has been set in the plot. This limit accounts for the difficulty of coiling longerons with large subtended angles, and sets an implicit limit on the maximum pressure loading, which depends on the length of the strip.

The previously made observations regarding Fig. 6, that the strips are limited by local shell buckling for shorter spans and larger subtended angles, and are deflection limited elsewhere, are still valid. In general, increasing the longeron

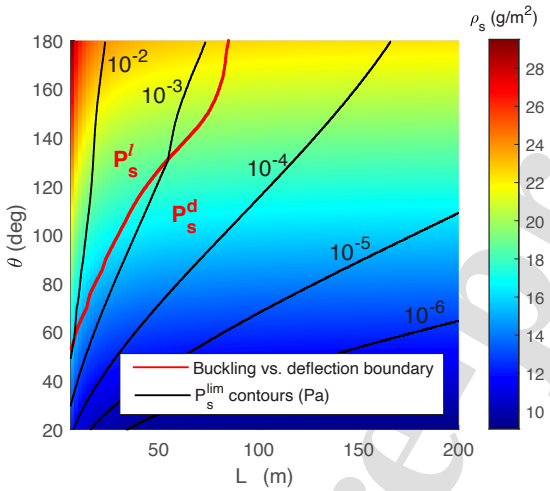

Figure 7: Areal density of strips as a function of span and longeron subtended angle. The red line marks the transition from deflection to buckling. Black lines mark order-of-magnitude variations of the pressure limit. The deflection limit is set to $w_s = 0.1L$.

angle and decreasing the span increases the pressure limit. Figure 7 also shows that to maintain the same pressure limit as the span increases, the strip's angle and mass must be scaled with the span.

4. Design Limits for Bending Architecture

This section presents an analysis of the forces in the booms and diagonal cables, which leads to a set of formulas to calculate the contribution of booms and cables to the overall areal density of the structure.

4.1. Analysis of Diagonal Booms and Cables

A standard reference architecture for studying the performance metrics of deployable booms is the tubular architecture (Mikulas et al., 2006). A particularly relevant architecture for the present study, known as Collapsible Tube Mast (CTM) or Omega Boom (Miura and Pellegrino, 2020), has been the main choice

for solar sails developed by the German Space Agency (DLR) and the NASA Langley Research Center (Block et al., 2011; Fernandez, 2017). Its cross-section is not exactly circular but can be closely modeled by a circle.

A diagonal boom, shown in Fig. 8, is modeled as a cantilevered thin-walled circular tube with cross-sectional radius r and thickness t. The tube is isotropic, with elastic modulus E and Poisson's ratio ν, density ρ, and second moment of area $I_b = \pi t r^3$. A diagonal cable, shown below the boom in the figure, is attached to the root and the tip of the boom. Since these structures are lightly loaded, extensional deformations are small and hence both booms and cables can be modeled as inextensible. Furthermore, limits on the maximum allowed deflections are imposed during the presents design process, and therefore standard small deflection assumptions are valid for the analysis.

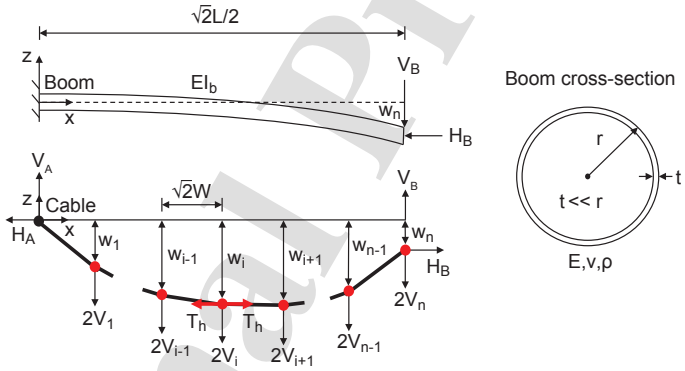

Figure 8: Bending architecture boom and cable parameters, boundary conditions, and reaction forces from strips under pressure loading P.

In Section 3.1 the strips were modeled as beams attached (simply supported) to the diagonal cables. The attachment nodes are denoted by red dots in Figs 4 and 8. There are n attachment nodes per cable, corresponding to the n strips in a quadrant. The node closest to the root ($i = 1$) supports the innermost strip and subsequent nodes correspond to strips farther out. The last node is at

the tip ($i = n$) and corresponds to the outermost strip, of length $L_n = L$. The spacing between the nodes is $\sqrt{2}W$.

The uniformly distributed loading PW on the beams is resisted by vertical reactions at the ith node:

$$V_i = \frac{1}{2} PW L_i \tag{8}$$

where $L_i = 2iW$. Since each node is connected to two identical strips, in adjacent quadrants, the vertical reaction is doubled, as shown in Fig. 8. The accompanying displacement of the cable is w_i.

It is assumed that there are no horizontal reaction components and the cable deflections are purely vertical. Hence, the horizontal component of the cable tension, T_h, is uniform throughout the cable. More details on the profile of the diagonal cables are provided in Appendix C.

Next, the analysis considers the diagonal boom, which is fixed at the root and is loaded by the cable tip reactions V_B (vertical) and H_B (horizontal), with $H_B = T_h$. The vertical tip force, V_B, is found by considering the moment equilibrium of the cable with respect to the root of the boom:

$$V_B = \frac{-w_n T_h}{\sqrt{2}Wn} + \sum_{i=1}^{n} \frac{2PW^2 i^2}{n} \tag{9}$$

The vertical deflection of the boom, w_b, is calculated by considering the bending deflection due to V_B, as well as the amplification factor $\frac{1}{1-T_h/T_{cr}}$ that accounts for the additional deflection caused by the axial compression T_h (Timoshenko and Gere, 1961). Therefore, w_b is given by:

$$w_b(x) = \frac{1}{1 - T_h/T_{cr}} \left[\frac{V_B x^2}{6EI_b} \left(\frac{3\sqrt{2}}{2} L - x \right) \right] \tag{10}$$

where T_{cr} is the fixed-free Euler buckling load:

$$T_{cr} = \frac{\pi^2 EI_b}{2L^2} \tag{11}$$

The maximum value of Eq. 10 occurs at the tip ($x = \sqrt{2}L/2$) and has the expression:

$$w_n = \frac{1}{1 - T_h/T_{cr}} \left(\frac{\sqrt{2} V_B L^3}{12EI_b} \right) \tag{12}$$

The final step in the analysis of the bending architecture is to calculate the horizontal component of the cable tension, T_h. Moment equilibrium of a free body of the cable extending from the root to the node $n-1$ yields:

$$T_h = \frac{PL^3}{2\sqrt{2}w_n n^3} \sum_{i=1}^{n-1} i^2 = H_B \tag{13}$$

The combined mass of boom and cables, m_b, is expressed in terms of the ratio between the mass of the cable, m_b^c, and the mass of the booms, m_b^b:

$$m_b = 4\sqrt{2}\pi r t \rho L \left(1 + \frac{m_b^c}{m_b^b}\right) \tag{14}$$

It is also convenient to define the linear mass density of the structure, m_b/L. Note that the linear mass density is not directly related to the density of a specific element of the structure, but is a useful metric nonetheless.

The boom thickness can be expressed as a function of the linear mass density and the ratio of the boom thickness and radius, $\frac{t}{r}$ (which can be taken to be constant). Therefore, the following expression is obtained:

$$t = \sqrt{\frac{\left(\frac{m_b}{L}\right)\left(\frac{t}{r}\right)}{4\sqrt{2}\pi\rho\left(1 + \frac{m_b^c}{m_b^b}\right)}} \tag{15}$$

Once t has been found by solving Eq. 15, the corresponding r is calculated for the chosen $\frac{t}{r}$.

4.2. Boom Design Limits

There are four design limits for the diagonal booms of the bending architecture.

The first limit corresponds to global buckling of the boom, which occurs when the axial compression, $H_B = T_h$, reaches the critical buckling load for a cantilevered beam-column. The corresponding pressure limit, P_b^g, is found by equating Eq. 13 to Eq. 11 and solving for P. The resulting expression is:

$$P_b^g = \frac{6\sqrt{2}\pi^3 E n^2 r^3 t w_n}{L^5 (n-1)(2n-1)} \tag{16}$$

The second limit corresponds to local buckling of the boom, which occurs when the maximum compressive stress reaches a critical value. The maximum

stress in the boom is the sum of the bending and axial stresses due to V_B and H_B, respectively, and hence is given by:

$$\sigma_b = \frac{M_b}{\pi r^2 t} + \frac{H_B}{2\pi r t} \tag{17}$$

The maximum bending moment occurs at the root and is given by:

$$M_b = \frac{\sqrt{2}}{2} L V_B + w_n H_B \tag{18}$$

The critical stress for combined bending and axial compression of a thin-walled circular cylinder is obtained from an interaction equation (Peterson et al., 1965) that incorporates knockdown factors that account for shell imperfections:

$$\sigma_{cl} = \frac{1}{\gamma_b}\left(\frac{M_b}{\pi r^2 t}\right) + \frac{1}{\gamma_c}\left(\frac{H_B}{2\pi r t}\right) \tag{19}$$

Here, σ_{cl} is the critical buckling stress of a cylindrical shell and has the expression (Brush and Almroth, 1975):

$$\sigma_{cl} = \frac{Et}{r\sqrt{3\left(1-\nu^2\right)}} \tag{20}$$

The knockdown factors for a cylindrical shell under pure bending, γ_b, and under pure axial compression, γ_c, are based on empirical curves in NASA SP-8007 (Peterson et al., 1965) and are a function of the radius to thickness ratio:

$$\gamma_b = 1 - 0.731\left(1 - e^{\frac{-1}{16}\sqrt{\frac{r}{t}}}\right) \tag{21}$$

$$\gamma_c = 1 - 0.901\left(1 - e^{\frac{-1}{16}\sqrt{\frac{r}{t}}}\right) \tag{22}$$

Substituting Eqs. 9, 13, 20, and 18 into Eq. 19 and solving for P results in the critical pressure P_b^l that induces local buckling of the boom:

$$P_b^l = \frac{8\sqrt{6}\pi E n^2 r t^2 w_n \gamma_b \gamma_c}{L^3\sqrt{1-\nu^2}\left(r\gamma_b\left(1-3n+2n^2\right)+2w_n\gamma_c\left(1+3n+2n^2\right)\right)} \tag{23}$$

The third limit corresponds to failure of the material at the point of highest stress in the boom's cross-section. The failure stress σ_f can be expressed as a function of the elastic modulus E and the failure strain ϵ_f:

$$\sigma_f = E\epsilon_f \tag{24}$$

Then, equating σ_b in Eq. 17 to σ_f in Eq. 24, with M_b given by Eq. 18 and v_b, H_B related to P by Eq. 9 and Eq. 13, leads to an equation that can be solved for P. The solution of this equation gives the pressure P_b^f that causes material failure at the root of the boom:

$$P_b^f = \frac{24\sqrt{2}\pi E n^2 r^2 t w_n \epsilon_f}{L^3\left(r\left(1-3n+2n^2\right)+2w_n\left(1+3n+2n^2\right)\right)} \tag{25}$$

The last design limit is related to the compliance of the structure. The maximum deflection of the boom, w_n is given by Eq. 12. The pressure P_b^d that causes the specific tip deflection w_n is found by substituting V_B, given by Eq. 9, into Eq. 12. Then, solving for P gives:

$$P_b^d = \frac{12\sqrt{2}\pi^3 E n^2 r^3 t w_n}{L^5\left(2+4n^2+n\left(\pi^2-6\right)\right)} \tag{26}$$

5. Design Limits for Cable-Stayed Architecture

This section provides a set of formulas to calculate the forces in the booms and cables and estimate their contribution to the overall areal density of the structure.

5.1. Analysis of Booms and Cables

It is assumed that in the cable-stayed architecture all booms have the same cross-sectional radius r_{cs} and thickness t_{cs}, Fig. 9. Hence, the second moment of area of the booms has the expression $I_{cs} = \pi t_{cs} r_{cs}^3$. The material properties of the booms are chosen identical to the booms of the bending architecture. Also, it is assumed that the booms, diagonal cables, and cable-stays are all inextensible and the deflection of the diagonal cables is assumed to be small. It follows from these assumptions that the diagonal booms are loaded in a purely axial mode, and all internal forces can be obtained from equations of equilibrium for any given maximum cable displacement.

The analysis follows similar lines to Section 4.1 and gives the following main results.

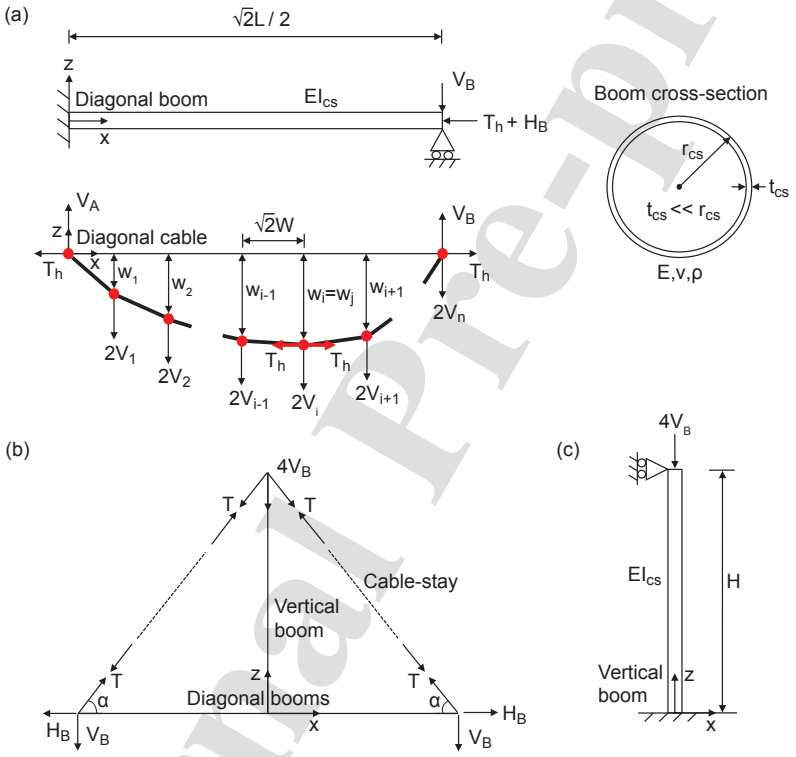

Figure 9: Components of cable-stayed architecture (a) horizontal booms and cables, (b) cable-stays, and (c) vertical boom.

The cable deflection converges to a cubic polynomial when the number of nodes $n \to \infty$ and the maximum deflection converges to:

$$w(x) \to \frac{3w_j x}{L^3}\sqrt{\frac{3}{2}}\left(L^2 - 2x^2\right) \tag{27}$$

where $j = \text{nint}\left(\frac{n}{\sqrt{3}}\right)$ and nint denotes the nearest integer function.
Horizontal component of diagonal cable tension:

$$T_h = \frac{PL^3}{2\sqrt{2}w_j n^3}\left(\sum_{i=1}^{n}\frac{i^2}{n}\left(n-j\right) - \sum_{i=1+j}^{n} i\left(i-j\right)\right) \tag{28}$$

Vertical and horizontal components of stay tension:

$$V_B = \frac{PL^2}{2n^3}\sum_{i=1}^{n} i^2 \tag{29}$$

$$H_B = \frac{V_B L}{\sqrt{2}H} \tag{30}$$

5.2. Boom Design Limits

There are six design limits for the diagonal and vertical booms in the cable-stayed architecture.

The first limit corresponds to global buckling of the diagonal booms. The diagonal booms are constrained in plane by the cable stays, but are able to buckle out of plane, as shown in Fig. 10. Therefore, their critical buckling load is calculated for the same fixed-free conditions considered in Eq. 11:

$$N_{cr}^{d} = \pi^2 \frac{EI_{cs}}{2L^2} \tag{31}$$

Equating N_{cr}^{d} in Eq. 31 to the sum of T_h in Eq. 28 and H_B in Eq. 30, and solving for the pressure provides the following expression for the pressure at which the diagonal booms will buckle:

$$P_{cs}^{d,g} = \frac{6\sqrt{2}\pi^3 E\hat{H}t_{cs}r_{cs}^3 n^3 w_j}{L^4\left(L\hat{H}j\left(n^2-j^2\right) + nw_j\left(1+3n+2n^2\right)\right)} \tag{32}$$

where $\hat{H} = \frac{H}{L}$.

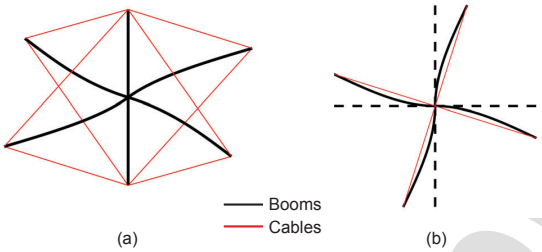

Figure 10: Buckling modes of diagonal booms in (a) perspective and (b) end views.

The second limit corresponds to global buckling of the vertical booms. They are modeled as fixed-pinned columns and their Euler critical load is given by (Timoshenko and Gere, 1961):

$$N_{cr}^{v} = \pi^2 \frac{EI_{cs}}{(0.699H)^2} \tag{33}$$

Setting N_{cr}^{v} in Eq. 33 equal to the axial compression of $4V_B$ in the vertical booms, given by Eq. 29, and solving for P yields the following expression for the pressure at which the vertical booms will buckle:

$$P_{cs}^{v,g} = \frac{6.140\ \pi^3 E t_{cs} r_{cs}^3 n^2}{L^4 \hat{H}^4 (1+n)(1+2n)} \tag{34}$$

The third and fourth limits correspond to local buckling of the diagonal and vertical booms, respectively. The procedure to obtain these limiting pressure values is similar to that outlined in Section 4.2 but in the present case the booms are loaded purely axially. The maximum stresses due to the axial forces $H_B + H_C$ and $4V_B$, respectively, are given by:

$$\sigma_{cs}^{d} = \frac{T_h + H_B}{2\pi r_{cs} t_{cs}} \tag{35}$$

$$\sigma_{cs}^{v} = \frac{4V_B}{2\pi r_{cs} t_{cs}} \tag{36}$$

Substituting Eqs. 28, 30 and 29 respectively for T_h, H_B and V_B in Eqs. 35 and 36 and then equating the resulting expressions to the critical buckling stress

for a cylindrical shell, Eq. 20, one obtains the following expressions for the values of P that result in the local buckling of the diagonal and vertical booms, respectively:

$$P_{cs}^{d,l} = \frac{8\sqrt{6}\pi E\hat{H}n^3 t_{cs}^2 w_j \gamma_c}{L^2\sqrt{1-\nu^2}\left(L\hat{H}j\left(n^2-j^2\right)+nw_j\left(1+3n+2n^2\right)\right)} \tag{37}$$

$$P_{cs}^{v,l} = \frac{2\sqrt{3}\pi E t_{cs}^2 n^2 \gamma_c}{L^2\sqrt{1-\nu^2}\left(1+n\right)\left(1+2n\right)} \tag{38}$$

where the knockdown factor γ_c has been introduced to account for imperfections.

The fifth and sixth limits correspond to material failure. The stresses in Eqs. 35 and 36, with Eqs. 28, 30 and 29 substituted respectively for T_h, H_B and V_B, are equated to the failure stress in Eq. 24. Then, solving for P provides the following expressions for the pressure corresponding to material failure, respectively for the diagonal and vertical booms:

$$P_{cs}^{d,f} = \frac{24\sqrt{2}\pi E\hat{H}n^3 r_{cs} t_{cs} w_j \epsilon_f}{L^2\left(L\hat{L}_v j\left(n^2-j^2\right)+nw_j\left(1+3n+2n^2\right)\right)} \tag{39}$$

$$P_{cs}^{v,f} = \frac{6\pi E r_{cs} t_{cs} n^2 \epsilon_f}{L^2\left(1+n\right)\left(1+2n\right)} \tag{40}$$

The smallest of the pressure limits in Eqs. 32, 34, 37, 38, 39, 40 is the actual limiting pressure for any specific design based on the cable-stayed architecture:

$$P_{cs}^{lim} = \min\left\{P_{cs}^{d,g}, P_{cs}^{v,g}, P_{cs}^{d,l}, P_{cs}^{v,l}, P_{cs}^{d,f}, P_{cs}^{v,f}\right\} \tag{41}$$

Here it should be noted that excessive compliance of the booms is not a meaningful limit for the cable-stayed architecture.

6. Optimal Designs

Designs based on the two architectures combine optimally designed strips and booms. The strips' longerons have the orthotropic properties in Table A.3 and are designed according to Section 3.2. The booms are assumed isotropic with modulus $E = 70$ GPa, density $\rho = 1600\,\mathrm{kg/m^3}$, and failure strain $\epsilon_f = 0.01$.

6.1. Optimal Bending Architectures

The limiting pressure for the booms is the smallest among the pressure limits given by Eqs. 16, 23, 25 and 26:

$$P_b^{lim} = \min\left\{P_b^g, P_b^l, P_b^f, P_b^d\right\} \tag{42}$$

Since the largest deflection of the strips occurs at the center of the outermost strip, the maximum deflection for the bending architecture is obtained by adding the maximum strip deflection, w_s, to the boom tip deflection, w_n. A deflection limit of $0.1L$, which may be acceptable for a solar array design, is chosen:

$$w = w_s + w_n = 0.1L \tag{43}$$

where different deflections of the strips and the booms can be considered as part of the design optimization.

As an example, $w_n = 0.05L$ has been chosen and the areal density needed to achieve this deflection limit together with specified values of P_b^{lim} has been computed for a range of side lengths. The procedure outlined in Appendix C for scaling the boom thickness and radius with respect to $\frac{m_b}{L}$ was applied. Note that the minimum length considered was $L = 6$ m, to match the strip length limit in Section 3.2, and that all booms within the design space were found to be limited by excessive compliance.

The results have been plotted in Fig. 11. The contribution of the booms and cables to the overall areal density of the structure is represented by the equivalent area density ρ_b, defined as:

$$\rho_b = m_b/L^2 \tag{44}$$

which has been plotted in Fig. 11.

Figure 12(a) presents the areal density of the booms and cables for three different values of the pressure limits, 10^{-2}, 10^{-3}, and 10^{-4} Pa, and for the boom tip deflection $w_n = 0.05L$. To satisfy Eq. 43, the maximum strip deflection limit is set to $w_s = 0.05L$ and the corresponding areal density of the strips is found using the procedure outlined in Section 3.2. Figure 12(b) shows plots of ρ_s vs.

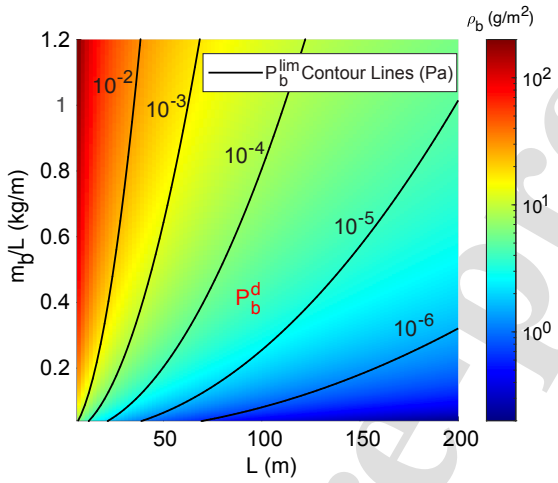

Figure 11: Areal density of booms and cables for bending architecture. Black lines mark order-of-magnitude variations of the pressure limit. The max. boom deflection and cable sag are $0.05L$.

L for the same three values of the pressure. Figure 12(c) shows a plot of the total areal density, also for the same pressures.

It should also be noted that, although there is no upper limit on the areal density of the booms and cables, the total areal density of the strips is constrained by the limit of 180° on the longeron subtended angles. This effectively results in a constraint on the maximum pressure/span that can be carried by the structure.

The effect of varying the allowable deflections of the booms and strips, while keeping the total maximum deflection equal to $0.1L$, has also been considered. By specifying $\frac{w_n}{L}$, the corresponding maximum strip deflection w_s was found from Eq. 43. Then, the procedure outlined in Section 3.2 was used to find the corresponding strip design limits. The results are shown in Fig. 13, where the contours provide the total equivalent areal density as a function of span and non-dimensionalized maximum boom deflection, for three different pressure limits.

In each plot, the specific boom deflection that corresponds to the highest mass efficiency has been identified by a red dot, for the full range of spans and for each chosen pressure. These optimal designs mostly correspond to an even distribution of the boom deflection vs. the strip deflection, but for the longest spans (on the right-hand side of the design space) the strip deflection tends to dominate and hence stiffer boom designs are required to satisfy the design limits.

6.2. Optimal Cable-Stayed Architectures

The mass of the horizontal and vertical booms, the diagonal cables, and the cable-stays is denoted by m_{cs} and is given by:

$$m_{cs} = 4\pi r_{cs} t_{cs} \rho L \left(\sqrt{2} + \hat{H}\right) \left(1 + \frac{m_{cs}^{c} + m_{cs}^{cs}}{m_{cs}^{d,v}}\right) \tag{45}$$

where the cable mass m_{cs}^{c} and cable-stay mass m_{cs}^{cs} are assumed to each be one tenth of the boom mass $m_{cs}^{d,v}$, i.e. $\frac{m_{cs}^{c}+m_{cs}^{cs}}{m_{cs}^{d,v}} = 0.2$. Equation 45 can be rearranged to express the boom thickness t_{cs} in terms of the linear mass density $\frac{m_{cs}}{L}$ (note that, as already noted for the bending architecture, the linear mass density is not the linear density of a specific structural element) the non-dimensionalized vertical boom length, and the boom's thickness to radius ratio:

$$t_{cs} = \sqrt{\frac{\left(\frac{m_{cs}}{L}\right)\left(\frac{t_{cs}}{r_{cs}}\right)}{4\pi\rho\left(\sqrt{2} + \hat{H}\right)\left(1 + \frac{m_{cs}^{c}+m_{cs}^{cs}}{m_{cs}^{h,v}}\right)}} \tag{46}$$

Equation 46 provides the scaling of the boom thickness in terms of $\frac{m_{cs}}{L}$ and $\hat{H}$ with a constant thickness to radius ratio. Once t_{cs} has been determined, the corresponding r_{cs} can be calculated from $\frac{t_{cs}}{r_{cs}}$.

A specific example is used to illustrate the design space. Consider a cable-stayed structure with $L = 20$ m and choose the maximum cable sag $w_j = 0.05L$, the thickness–to-radius ratio $\frac{t_{cs}}{r_{cs}} = 0.03$, and set the linear mass density to $\frac{m_{cs}}{L} = 0.1$ kg/m. These values of the linear mass density and thickness to radius ratio are reasonable for tubular booms (Greschik and Mikulas, 2002).

The limiting pressure from Eq. 41 has been plotted in Fig. 14 as a function of the only remaining design variable, $\hat{H}$. The plot shows the interaction of

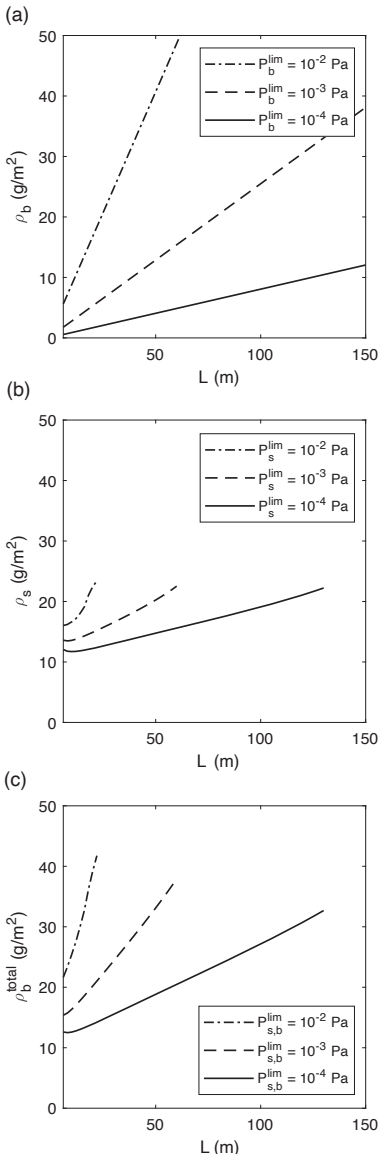

Figure 12: Areal densities for bending architecture (a) booms and cables, (b) strips, and (c) total vs. span L for three pressure limits. The max. boom deflection, cable sag, and strip deflection are $0.05L$ and the total max. deflection is $0.1L$.

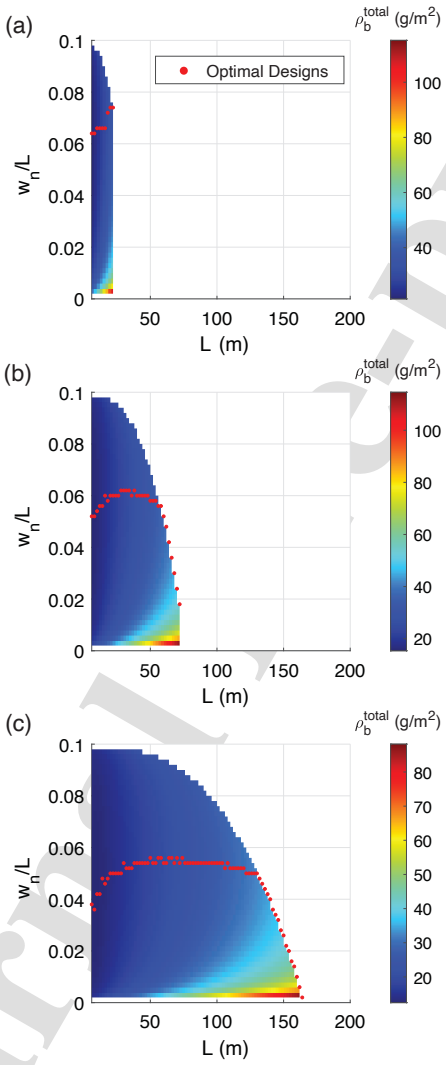

Figure 13: Total areal density for bending architecture vs. span and non-dimensionalized max. boom deflection for the pressure limits of (a) 10^{-2} Pa, (b) 10^{-3} Pa, and (c) 10^{-4} Pa. The red dots indicate the minimum density designs. The total max. deflection limit is $0.1L$.

two limiting conditions, i.e. global buckling of either the horizontal or vertical booms. The transition occurs at $\hat{H} = 1.683$. For $\hat{H} > 1.683$ the vertical boom will buckle at lower pressures than the horizontal boom, and vice versa. The most important result from this plot is that it identifies an optimal design which carries the largest pressure, $P_{cs}^{lim} = 0.0238$ Pa. The corresponding value of the non-dimensionalized vertical boom height is $\hat{H} = 0.392$.

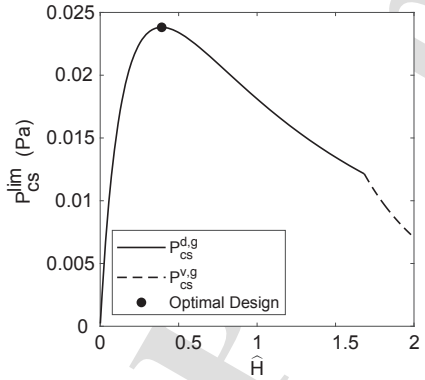

Figure 14: Pressure limit P_{cs}^{lim} for cable-stayed architecture booms as a function of non-dimensionalized vertical boom length, for span $L = 20$ m and linear mass density $\frac{m_{cs}}{L} = 0.4$ kg/m. The max. cable sag is set to $w_j = 0.05L$.

The same analysis to find the optimal boom designs was repeated for the range of spans $6 \leq L \leq 200$ m and the results are shown in Fig. 15 as a contour plot of the limiting pressure as a function of L and $\hat{H}$. The optimal $\hat{H}$ for each span is shown by a black line. The red line in the plot marks the transition between the global buckling of the horizontal and vertical booms. Since the optimal designs correspond to values of $\hat{H}$ lower than the buckling transition, they are all limited by global buckling of the horizontal booms.

Note that the value of the optimal $\hat{H}$ remains almost constant when L is increased. This is because the boom radius and thickness have to remain constant as the linear mass density has been fixed.

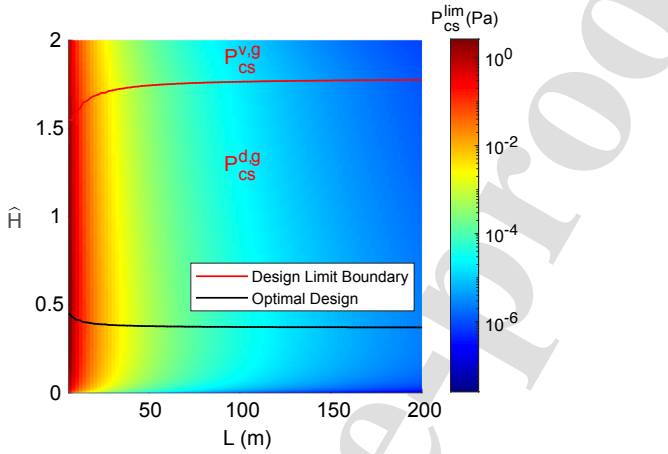

Figure 15: Pressure limits for cable-stayed architecture booms as a function of span for $\frac{m_{cs}}{L} = 0.4$ kg/m and max. cable sag $w_j = 0.05L$. The red line marks the transition between two different limiting conditions. The black line indicates the maximum pressure.

For a more general characterization of the optimal designs, a range of linear mass densities was considered, in order to allow a wider range of pressure limits. This was done by repeating the analysis that generated Fig. 15, for a range linear mass density values and selecting from each analysis the optimal value of P_{cs}^{lim}. All designs were found to be limited by global buckling of the horizontal boom, as was already the case in Fig. 15. Then, the corresponding equivalent areal density (of the booms and cables only) was calculated from:

$$\rho_{cs} = m_{cs}/L^2 \tag{47}$$

and the density variation has been plotted in terms of L and $\frac{m_{cs}}{L}$ in Fig. 16. Since the linear mass density has been allowed to vary, the boom radius and thickness can also vary. Hence, by following one of the constant-pressure black lines, one follows the evolution of the optimal design when L is increased.

The above analysis has obtained the optimal boom and cable designs for the cable-stayed architecture. Next, this result was combined with the optimal

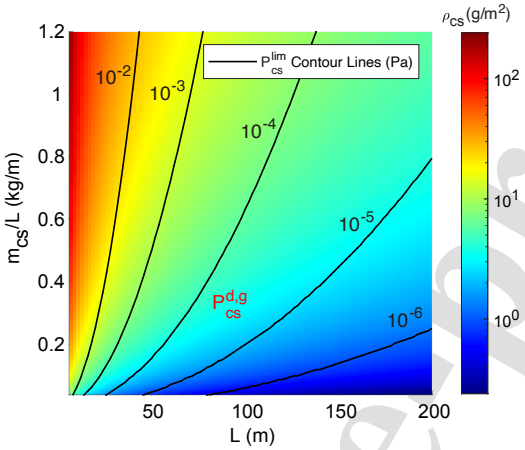

Figure 16: Areal density of optimal cable-stayed architecture booms and cables as a function of span and linear mass density. The black lines mark order-of-magnitude variations of the pressure limit. The max. cable sag is $w_j = 0.05L$. All designs are limited by global buckling of the horizontal booms.

design for the strips, presented in Section 3.2.

The total maximum deflection limit was set to $w_{cs} = 0.1L$, which is identical to the deflection limit for the bending architecture, in Section 6.1. However, since the tip deflection of the diagonal booms is zero in this architecture (recall that the booms, the diagonal cables, and the cable stays are all assumed inextensional) the location of the maximum cable sag is at the node nearest to $x = L/\sqrt{6}$ (see Eq. 27 in Section 5.1) along the diagonal x axis, while the maximum strip deflection is —as before— at the center of the outermost strip. The distribution of deflections between the diagonal cables and the strips along with the applied pressure and the values of all design parameters need to be considered to determine the total maximum deflection. This analysis was carried out by choosing a specific value for the maximum cable sag, w_j as shown in Fig. 9 (a), and then determining the specific strip design such that the total maximum deflection is $0.1L$. In practice, this involves finding the longeron

subtended angle for which the strip deflection has the required value. The same pressure used in the analysis of the booms was also used for the analysis of the strips.

The deflection at the center of a general strip i can be expressed in terms of a coordinate x along the diagonals. The strip length is $L_i = \sqrt{2}x_i$ and the strip deflection is:

$$w_i(x) = \frac{5PWx_i^4}{96EI_s} \tag{48}$$

Adding the deflection of the diagonal cable, given by Eq 27, gives the total deflection at the center of strip i:

$$w_{cs}(x_i) = \frac{3w_j x_i}{L^3}\sqrt{\frac{3}{2}}\left(L^2 - 2x_i^2\right) + \frac{5PWx_i^4}{96EI_s} \tag{49}$$

Setting w_{cs} in Eq. 49 equal to deflection limit $w_{cs} = 0.1L$ and solving for the strip longeron stiffness gives:

$$EI_s(x_i) = \frac{25PWL^3x_i^4}{48\left(L^4 - 15\sqrt{6}L^2w_jx_i + 30\sqrt{6}w_jx_i^3\right)} \tag{50}$$

For any optimal boom and cable design, the corresponding values of P_{cs}^{lim}, w_j, and L are inputted into Eq. 50. Then, the required bending stiffness for the strips is chosen as the maximum over all values of i: $\max\{EI_s(x_i)\}$. The choice of this value ensures that the condition $w_{cs} = 0.1L$ is satisfied for all strips.

Finally, equating $\max\{EI_s(x_i)\}$ to Eq. 2 and solving for θ yields the value of the longeron subtended angle, θ_s^d, needed to satisfy the total maximum deflection limit. In practice, it is faster to consider x instead of x_i, hence using a continuous form of Eq. 50 to find θ_s^d.

To complete, the above design based on the deflection limit for the strips is compared to a design that meets the buckling limit. For any specified pressure limit P_{cs}^{lim} and span L, the required maximum bending moment occurs at the center of the outermost strip. Then, the corresponding value of the longeron subtended angle, θ_s^l, is obtained from Fig. B.22. Hence, the actual value of the longeron subtended angle is the largest of the two values:

$$\theta_s^{lim} = \max\left\{\theta_s^d, \theta_s^l\right\} \leq 180^\circ \tag{51}$$

Once θ_s^{lim} has been determined, the areal density of the strips, ρ_s, is computed with Eq. 5, and the computation is repeated over a range of spans, pressures, and deflection limits.

Finally, the areal density of the booms, cables, and cable-stays is added to the areal density of the strips over the full range of pressure limits and spans:

$$\rho_{cs}^{total} = \rho_{cs} + \rho_s \tag{52}$$

The results of these calculations have been plotted in Fig. 17 for the pressure limits 10^{-2}, 10^{-3}, and 10^{-4} Pa, assuming that the maximum cable sag is $0.05L$ and the total maximum deflection limit is $0.1L$. Similarly to the bending architecture, there is no limit on the values of ρ_{cs}, but the total areal density ρ_s and ρ_{cs}^{total} are constrained to the spans for which $\theta \leq 180°$.

This analysis has been repeated by varying the maximum deflection ratio between the strips and the diagonal cables. The results are shown in Fig. 18, again for three values of the pressure limits. The minimum total areal densities for each span have been marked with red dots. These points identify the most mass efficient values of $\frac{w_j}{L}$ until the upper limit for the span is reached for each pressure limit. Overall, these optimal designs tend to favor larger cable displacements and smaller strip deflections.

7. Comparison

The total areal densities of the optimized designs based on the bending and cable-stayed architectures have been presented in Fig. 13 and Fig. 18, for a range of spans, for three different pressure limits, and for a total maximum deflection limit set to ten percent of the span. The same results have been summarized in Fig. 19(a), where any designs with a boom thickness lower than 0.1 mm are indicated by a dotted line. These designs are confined to shorter spans and lower pressure limits. Note that, for a given pressure limit, initially the areal density increases linearly with the span. At some point, the curve reaches a vertical asymptote, indicating a rapid increase in density, when the

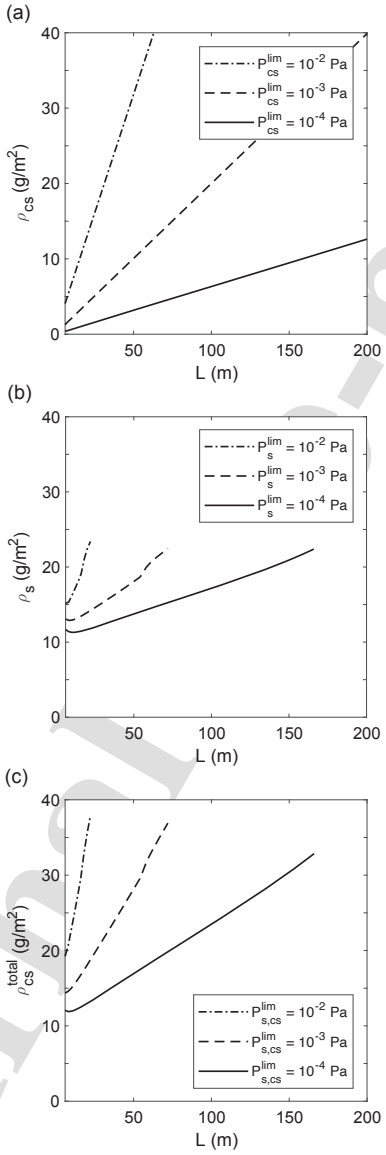

Figure 17: Areal density of cable-stayed architecture's (a) booms and cables, (b) strips, and (c) total vs. span for three pressure limits. The max. cable sag is $0.05L$ and the total max. deflection limit is $0.1L$.

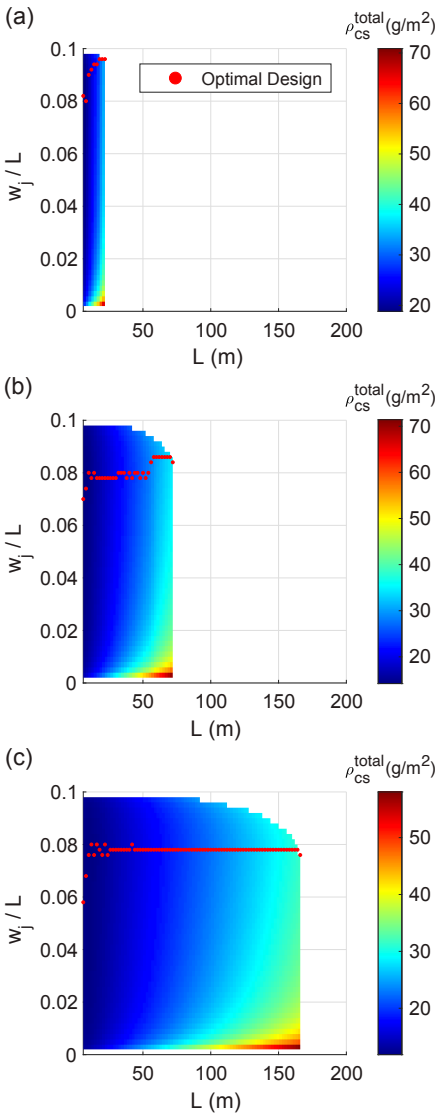

Figure 18: Total areal density for cable-stayed architecture as a function of span and non-dimensionalized max. cable sag for the pressure limits (a) 10^{-2} Pa, (b) 10^{-3} Pa, and (c) 10^{-4} Pa. The red dots indicate the minimum areal density for each span. The total max. deflection limit is $0.1L$.

architecture reaches its limit. This is associated with the limit on the strip longeron angle $\theta < 180°$.

Figure 19(a) shows that the cable-stayed architecture is more efficient than the bending architecture. The difference in efficiency between the two architecture has been highlighted by plotting the areal density ratio, in Fig. 19(b). This ratio is closer to one for the shorter spans considered and tends to further decrease for longer spans, with the exception of the case $P = 10^{-2}$ Pa. The general trend, for structures with smaller deflection limits, is that the superior performance of the cable-stayed architecture tends to get even better for longer spans.

The maximum possible span for a given pressure is governed by the longerons reaching the maximum subtended angle $\theta = 180°$. This occurs at the same span for both architectures, although in the case of the cable-stayed architecture reaching the angle limit occurs suddenly, whereas in the bending architecture the areal density starts to increase more rapidly, as stiffer and heavier booms are used to compensate for the increasing compliance of the strips. This can be clearly seen in Fig. 13(b) and (c) where, beyond a certain value of L, the optimal designs are forced to rapidly decreasing tip deflections in order to maintain the overall deflection limit. This behavior is not observed for the cable-stayed architecture because the optimal specified cable sag $\frac{w_j}{L}$ remains fairly constant over the entire range of spans, as can be seen Fig. 18.

In Fig. 19(a), the circles indicate designs for which the strips are limited by local shell buckling while a curve without circles indicates that the strips have reached the deflection limit. Note that the cable-stayed architecture is more susceptible to strip buckling than the bending architecture, and buckling generally occurs for larger pressures and values of L closer to the maximum value.

The diagonal booms of the bending architecture are limited by deflection, whereas the booms of the cable-stayed architecture are limited by global buckling.

The effects of lowering the maximum deflection limit to $0.05L$ and also $0.01L$

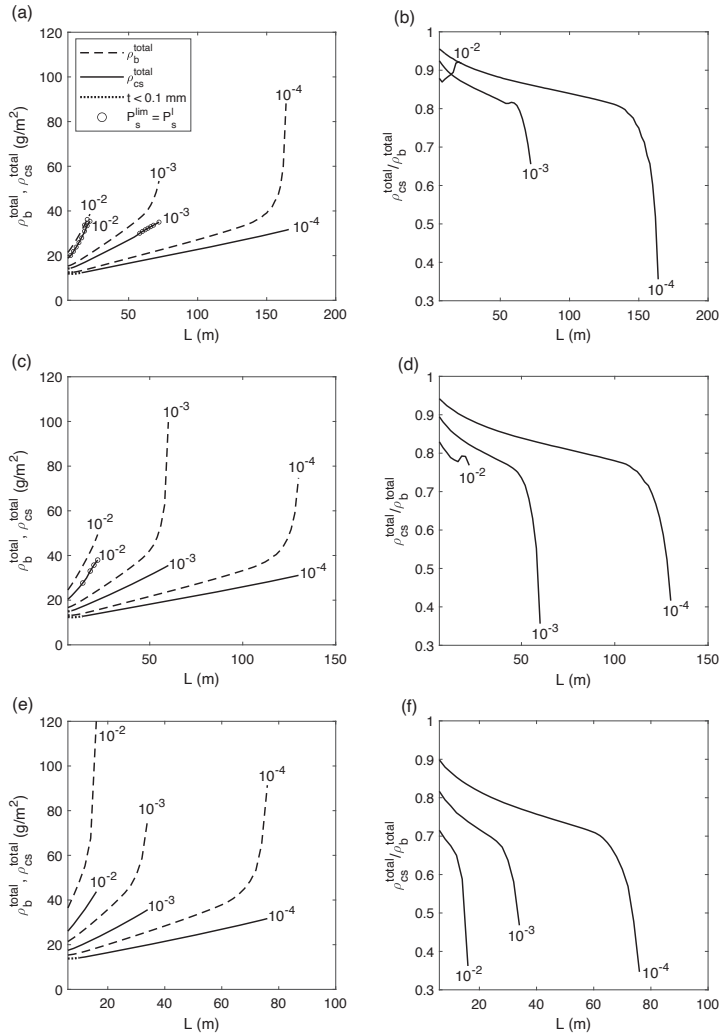

Figure 19: Total areal densities for bending and cable-stayed architectures, and their ratios, for the pressure limits of 10^{-2} Pa, 10^{-3} Pa, and 10^{-4} Pa. The total max. deflection limit is (a, b) $0.1L$, (c, d) $0.05L$, and (e, f) $0.01L$. Designs with boom thickness less than 0.1 mm are shown with dotted lines. Designs limited by buckling rather than excessive deflection are shown by circles.

were considered and the results are shown in Figs. 19(c) and (e), respectively. The corresponding areal density ratios are shown in Figs 19(d) and (f). Note that the areal density trends and the boom design limiting conditions described above for the $0.1L$ deflection limit are unchanged at these lower deflections.

It is interesting to compare the areal density trends when the total maximum deflection limit is decreased from $0.1L$ to $0.01L$, Figs 19(a) vs. (e) and Fig. 19(b) vs. (f). For the smaller deflection, the cable-stayed architecture becomes even more mass efficient than the bending architecture.

This is because lowering the deflection limit imposes stricter restrictions on mass minimized designs for the bending architecture, whose booms are always limited by excessive deflection. The booms must have larger cross-sections to withstand the same pressure loading with smaller deflections, which increases the required mass. The areal density for the cable-stayed architecture also increases as the deflection limit is lowered, but by a lesser amount when compared to the bending architecture. Lowering the deflection limit also decreases the maximum acceptable lengths for both architectures when the strips are limited by excessive deflection. This is because at the maximum longeron subtended angle of 180°, the strips reach the lowered deflection limit at smaller lengths. Finally, the number of design points where the strips are limited by buckling decreases as the deflection limit is lowered because they will become excessively deflected before buckling.

7.1. Example

Two optimal designs for a structure with span $L = 40$ m that is required to carry a pressure $P = 10^{-3}$ Pa with a deflection limit of $0.1L = 4$ m are presented.

The corresponding designs are chosen for the bending and cable-stayed architectures in Fig. 19(a). The values of the boom length, radius, and thickness, as well as the strip longeron angle and total areal density are listed in Table 2.

The higher mass efficiency of the cable-stayed architecture leads to an optimal design with areal density of 23.8 g/m^2 compared to the bending architec-

ture's 28.4 g/m^2. The cable-stayed architecture's boom radius, thickness, and longeron angle are smaller than those of the bending architecture, resulting in greater mass efficiency despite the additional mass introduced by the vertical booms and cable-stays.

Table 2: Geometry, areal density, and design limiting conditions for optimal bending and cable-stayed architectures with $L = 40$ m, $P^{lim}_{s,b,cs} = 10^{-3}$ Pa, and $w = 0.1L$.

Architecture	H (m)	r, r_{cs} (mm)	t, t_{cs} (mm)	θ (deg)	$\rho^{total}_{b,cs}$ (g/m^2)
Bending	N/A	20.1	0.6	130.2	28.4
Cable-stayed	18.5	14.5	0.43	104.1	23.8

For both designs, the strips are limited by excessive deflection. The bending architecture booms are also limited by excessive deflection while the cable-stayed architecture is limited by global buckling of its diagonal booms. The deflected shapes under the pressure 10^{-3} Pa are shown in Fig. 20. There are $n = 20$ strips per quadrant and the total maximum deflection of 4 m is confirmed to be at the center of the outermost strips ($i = 20$) for the bending architecture and the center of strip $i = 18$ for the cable-stayed architecture.

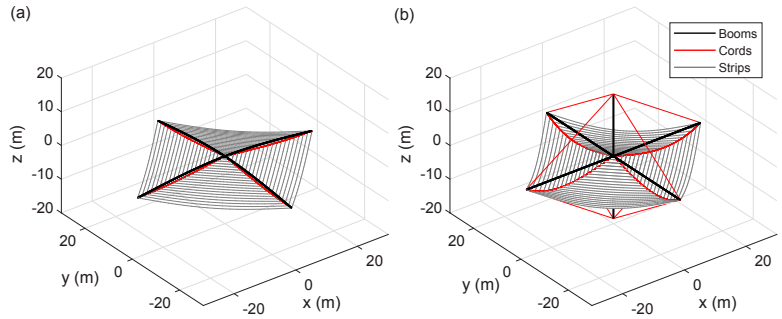

Figure 20: Deflected shapes of optimal (a) bending and (b) cable-stayed architectures from Table 2.

8. Conclusion

It is generally known that structures that carry loads by bending have lower mass efficiency than structures loaded purely in tension/compression, however in practical applications it is important to quantify the difference. The present comparison between different structural architectures has done this, in a way that is both quantitative and systematic. It has also provided a general approach and methodology to enable more rational choices between different structural concepts and thus improve the design process in the future.

The present study has focused on two structural concepts for large square space structures. A detailed procedure has been presented, and summarized in Fig. 3, for considering all of the relevant design limits and obtain the optimal values of the design parameters. It has made it possible to accurately estimate the best achievable areal density for these structures.

It has been shown that the cable-stayed architecture is more mass efficient than the bending architecture across the whole design space considered in the study. The difference in efficiency is not constant, but varies with the load magnitude and span of the structures as shown in Figs. 19(b, d, f) and, specifically, it increases for larger spans and pressures. Lowering the maximum deflection limit imposes a harsher mass penalty on the bending architecture and this further raises the relative performance of the cable-stayed architecture. Upper limits on span are found to be driven by excessively deflected strips and this limit becomes more restrictive as the architecture's load carrying capacity increases. The cable-stayed architecture is also more susceptible to strip buckling than the bending architecture at larger pressure limits. For the booms, the bending and cable-stayed architecture are limited by deflection and by global buckling of the horizontal booms, respectively.

These results are of practical importance in several different ways. First, the efficiency gain afforded by the more complex, cable-stayed architecture is relatively small in many cases, and may not be justified in a comprehensive trade study. For example, the mass efficiency gain is less than 12% for structures with

span up to 50 m designed for a pressure load of 10^{-4} Pa and for a deflection limit of $10\%L$. Second, the specific areal density values that have been obtained in the present study, e.g. less than 15 g/m^2 for the above case, set a challenge for the implementation of future deployable structures. Then, an important question will be how to test such ultralightweight structures in the presence of gravity.

As a final point, it is noted that in the present study it was assumed that the diagonal booms are circular in both architectures, but it should be noted that this assumption results in a penalization of the cable-stayed architecture. Because the stays constrain the tip deflection of a boom within the plane defined by the boom and the stay, but do not constrain the out-of-plane deflection of the tip, the buckling load in Eq. 31 was calculated for fixed-free end conditions. By increasing the out-of-plane stiffness of the diagonal booms, e.g. by choosing booms with a lenticular cross-section instead of a circular one, a fixed-supported end condition would result and hence the buckling load of the boom would be increased significantly. With this small change, the mass efficiency gain would be increased to 22% for the above considered case, of structures with span up to 50 m designed for a pressure load of 10^{-4} Pa and a deflection limit of $10\%L$. Even higher gains would be obtained for lower deflection limits and higher pressures.

Acknowledgements

The authors thank Dr. Martin Mikulas of the National Institute of Aerospace for insightful discussions. Financial support from the Space Solar Power Project at the California Institute of Technology is gratefully acknowledged.

References

Arya, M., Lee, N. and Pellegrino, S., 2016. Ultralight Structures for Space Solar Power Satellites. SciTech 2016, San Diego, AIAA-2016-1950.

Banik, J.A., Maji, A.K., 2016. Structural scaling parameters for rectangular flexible blanket solar arrays. Journal of Spacecraft and Rockets 53, 936–951.

Belvin, W.K., 1984. Analytical and experimental vibration and buckling characteristics of a pretensioned stayed column. Journal of Spacecraft and Rockets 21, 456–462.

Block, J., Straubel, M. and Wiedemann, M., 2011. Ultralight deployable booms for solar sails and other large gossamer structures in space. Acta Astronautica, 68(7-8), pp. 984-992.

Brush, D.O., Almroth, B.O., 1975. Buckling of bars, plates, and shells. McGraw-Hill, New York.

Budiansky, B., 1999. On the minimum weights of compression structures. International Journal of Solids and Structures 36, 3677–3708.

Campbell, T. G., Hoop/column antenna technology development summary, Large Space Systems Technology, volume 1, 1981

Feria, V., Lou, M., Huang, J., Speer, S., 1998. Lightweight deployable space radar arrays, in: 39th AIAA/ASME/ASCE/AHS/ASC Structures, Structural Dynamics, and Materials Conference and Exhibit, p. 1933.

Fairclough, H. E., Gilbert, M., Pichugin, A.V., Tyas, A. and Firth, I., 2018. Theoretically optimal forms for very long-span bridges under gravity loading. Proceedings of the Royal Society part A. 474 (2017.0726).

Fernandez, J.M., 2017. Advanced deployable shell-based composite booms for small satellite structural applications including solar sails. In International Symposium on Solar Sailing 2017 (No. NF1676L-25486).

Gdoutos, E., Truong, A., Pedivellano, A., Royer, F., Pellegrino, S., 2020. Ultralight deployable space structure prototype, AIAA Scitech 2020 Forum, AIAA-2020-0692.

Greschik, G., Mikulas, M., 2002. Design study of a square solar sail architecture. Journal of Spacecraft and Rockets 39, 653–661.

Heard Jr, W.L., Bush, H.G., Walz, J.E., Rehder, J.J., 1981. Structural sizing considerations for large space platforms. Journal of Spacecraft and Rockets 18, 556–564.

Hedgepeth, J., 1981. Critical requirements for the design of large space structures, in: 2nd Conference on Large Space Platforms: Toward Permanent Manned Occupancy in Space, p. 443. Also in NASA-CR-3484.

Keck Institute of Space Studies (KISS), 2022. Non-Nuclear Exploration of the Solar System. Brophy, J., Pellegrino, S., and Lubin, P. , eds. Final Workshop Report for the W.M. Keck Institute for Space Studies, Pasadena, CA.

Leclerc, C., 2020. Mechanics of ultra-thin composite coilable structures. Ph.D. thesis. California Institute of Technology.

Leclerc, C., Pellegrino, S., 2019. Reducing stress concentration in the transition region of coilable ultra-thin-shell booms, in: AIAA Scitech 2019 Forum, AIAA-2019-1522.

Leclerc, C., Pellegrino, S., 2020. Nonlinear elastic buckling of ultra-thin coilable booms. International Journal of Solids and Structures 203, 46–56.

Matousek, S., 2007. The Juno New Frontiers mission. Acta Astronautica 61, 932–939.

Miura, K., Pellegrino, S. 2020. Forms and Concepts for Lightweight Structures, Cambridge University Press.

Mikulas, M.M., Collins, T.J., Doggett, W., Dorsey, J. and Watson, J., 2006. Truss performance and packaging metrics. In AIP Conference Proceedings (Vol. 813, No. 1, pp. 1000-1009). American Institute of Physics.

Murphey, T.W., Banik, J., 2011. Triangular rollable and collapsible boom. US Patent 7,895,795.

Peterson, J.P., Seide, P., Weingarten, V.I., 1965. Buckling of thin-walled circular cylinders. NASA SP-8007.

Royer, F., Pellegrino, S., 2022. Probing the stability of ladder-type coilable space structures, AIAA Journal, 60, 2000-2012.

Thomas, V.C., Makowski, J.M., Brown, G.M., McCarthy, J.F., Bruno, D., Cardoso, J.C., Chiville, W.M., Meyer, T.F., Nelson, K.E., Pavri, B.E., et al., 2011. The Dawn spacecraft. Space Science Reviews 163, 175–249.

Timoshenko, S.P., Gere, J.M., 1961. Theory of Elastic Stability. Dover Publications.

Appendix A. Details of Strips

Specific dimensions and properties for the strips were based on the Caltech SSPP structure (Royer and Pellegrino, 2020). The strip width, defined as the distance between the longeron inner edges was chosen as $W = 1.0$ m. The length of the battens was increased to 1.012 m, to provide 6 mm overlaps with the longeron webs. The dimensions of the batten cross-section were $h = 0.6$ mm and $b = 3$ mm. The longeron web width was set to $d = 8$ mm and the flange thickness to $t_f = 85.5$ μm.

The radius R of the flange cross-section was chosen as the smallest value that allows flattening of the longerons, in order to allow coiling of the longerons (Leclerc and Pellegrino, 2019). A transverse strain limit $\epsilon_f = 1\%$ was assumed for the flange laminate, which was reduced to 0.5% to allow for strain localization during coiling of the longerons. Hence, the longeron radius was obtained from the strain-curvature relation for transverse bending of the flange:

$$R = \frac{t_f}{2\epsilon_f} = 8.5 \text{ mm}. \tag{A.1}$$

The universal value $R = 8.5$ mm was assumed throughout this study, for all values of the structural span L.

The remaining geometric parameter is the angle θ subtended by the flanges of the longerons, which is chosen as the primary design variable for the strips.

The flange layup is $[\pm 45_{GFPW}/0_{CF}/\pm 45_{GFPW}]$, where $GFPW$ denotes a glass fiber plain-weave ply and CF denotes a unidirectional carbon fiber ply. The single ply thicknesses are $t_{CF} = 35.5$ μm and $t_{GFPW} = 25$ μm. In the webs, an additional $\pm 45^{\circ}_{GFPW}$ ply is added between the two flange laminates. The unidirectional carbon fiber composite for the battens is the same as that used in the flanges. The laminate $\boldsymbol{ABD}$ stiffness matrices Leclerc and Pellegrino (2020) are presented in Table A.3. Note that $\boldsymbol{B}=\boldsymbol{0}$.

Table A.3: Laminate stiffness coefficients.

	A_{11}	A_{12}	A_{22}	A_{66}	D_{11}	D_{12}	D_{22}	D_{66}
	N/mm				Nmm			
Flange	5,432	619	942	737	1.076	0.482	0.781	0.459
Web	11,369	1,512	2,269	1,727	28.2	4.32	7.44	4.93

The longeron laminate was kept fixed throughout this study, although thicker laminates may be advantageous for structures with longer spans.

Appendix B. Buckling of Strips

The transverse pressure P on the strips puts the upper flanges of the longerons under compression and, due to the small thickness of the flanges, local buckling can occur.

The values of P at which buckling of the flanges occurs were calculated, for strips of lengths $L = 1 - 20$ m and for subtended angles $\theta = 45 - 180^{\circ}$. with the Abaqus/Standard 2020 finite element software. Geometric nonlinearity in the prebuckling regime was accounted through an iterative solution of the buckling problem, following Royer and Pellegrino (2020).

The longerons and battens were modeled with 4 node reduced integration shell elements (S4R) and linear 3D beam elements (B31), respectively. The finite element mesh was uniform with an element size of 2 mm for both the shell and

beam elements. The strip was constrained against translation in all directions at one corner (pinned), and in the vertical direction only at the remaining three corners. In addition, in-plane translations were constrained at two corners, to prevent rigid-body rotations around the pinned corner. No rotational degrees of freedom of the structure were constrained.

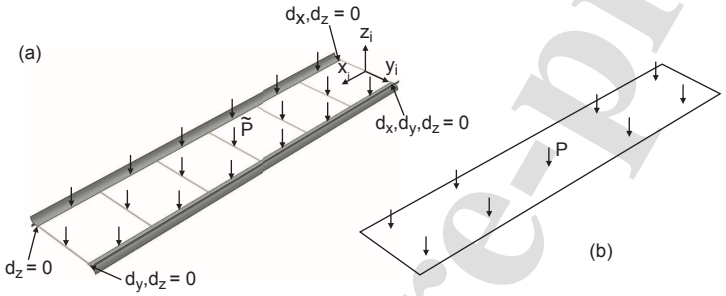

Figure B.21: Finite element model of a strip, showing (a) uniform pressure $\tilde{P}$ on longerons and battens in and (b) equivalent pressure P on whole strip.

In the finite-element analysis, a uniform pressure $\tilde{P}$ was applied on the top faces of the longeron webs and battens, over a total area $\tilde{A}$ as shown in Fig. B.21(a). The equivalent pressure on the complete strip, Fig. B.21(b), accounts for a non-structural infill panel attached to the battens and was calculated from:

$$P = \tilde{P}\frac{\tilde{A}}{A} \tag{B.1}$$

The equivalent pressure that causes local buckling of a strip, P_s^l, was computed for strips of different lengths and longeron subtended angles θ. The bending moment at mid-span was calculated from:

$$M_s^l = \frac{1}{8}P_s^l W L_i^2 \tag{B.2}$$

and it was found that for a wide range of lengths the maximum buckling moment is effectively independent of the strip length.

This is an important result for the design of the strips, as varying the strip length does not vary the local buckling moment. Hence, since the longeron sub-

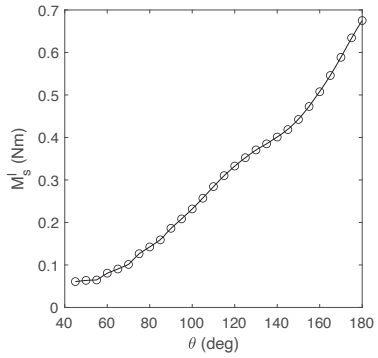

Figure B.22: Buckling moment of strips of any length greater than 5 m, and for a range of subtended angles.

tended angle is the primary design variable for the strips, the buckling bending moment was computed for a specific strip length and for the range of angles $45° \leq \theta \leq 180°$, in 5° increments. The resulting variation of the buckling moment is shown in Fig. B.22.

Appendix C. Cable Profile in Bending Architecture

The vertical cable displacement at the ith node, w_i, is related to the displacements of the two adjacent nodes by an equation of equilibrium for a section of the cable:

$$2w_i - w_{i+1} - w_{i-1} = \frac{2\sqrt{2}iPW^3}{T_h} \tag{C.1}$$

where $w_0 = 0$ at the root attachment point and w_n is equal to the boom tip deflection, given by Eq. 12. To match the tip deflection, w_n is specified as an input along with the pressure P. Then the unknowns for the cable include the deflections $w_1, ..., w_{n-1}$ and the horizontal tension component T_h. They are obtained by solving $n-1$ equilibrium equations based on Eq. C.1, together with Eq. 12.

The cable displacements have to be such that the total maximum deflection of the structure formed by the strips, cables and booms is equal to the deflection design limit.

Figure C.23(a) shows three configurations of a cable hanging from a boom. The two extreme configurations correspond to: a lightly tensioned cable that deflects more than the boom tip ($w_{n-1} > w_n$), and a highly tensioned cable that deflects less than the boom tip ($w_{n-1} < w_n$). The latter design requires a heavier boom to carry the higher cable force while avoiding boom buckling.

To keep a consistent cable profile, a mass efficient design is obtained for the case $w_{n-1} = w_n$ and this is the choice made for the rest of the paper. While the lightly tensioned cable configuration ($w_{n-1} > w_n$) yields a lighter boom, the mass savings are small, and the cable deflection becomes asymptotically unbounded as it approaches the limit shown by the dashed line in Fig. C.23 (a). To avoid this effect, the $w_{n-1} = w_n$ configuration is chosen.

Figure C.23(b) shows a plot of the linear density of the structure for different spans, for the following specific design parameters: $\frac{t}{r} = 0.03$, $P = 10^{-4}$ Pa, and $w_n = 0.05L$. The booms were chosen isotropic for simplicity, with $E = 70$ GPa and $\rho = 1600$ kg/m^3. These values are comparable to composite materials commonly used in deployable booms. The cable mass was set to one tenth of the boom mass (i.e. $m_b^c/m_b^b = 0.1$), which is a conservative estimate for a cable design that undergoes small axial strains.

In Fig. C.23(b), the solid line corresponds to the above described mass efficient design. The designs with higher cable tension correspond to the region above the solid line and correspond to heavier boom-cable systems. The dashed line shows the designs for which the cable deflection $w_{n-1} \to \infty$ as the cable tension $T_h \to 0$. Below this limit lie imaginary solutions for the cable displacement.

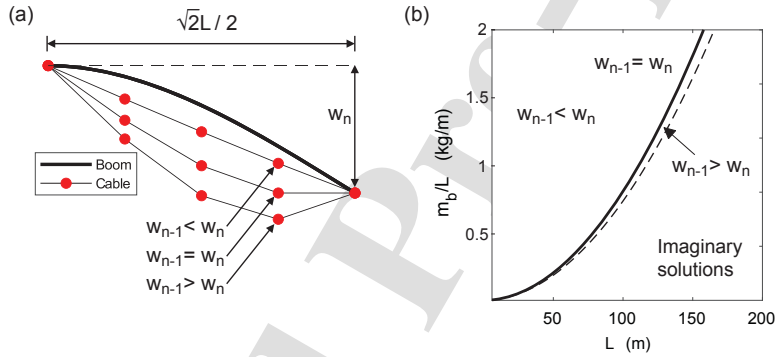

Figure C.23: (a) Three design approaches for boom-cable system. (b) Linear mass density of a boom and cable pair in the bending architecture as a function of L, when varying the max. cable deflection with respect to boom tip deflection. The pressure loading is $P = 10^{-4}$ Pa and the max. boom deflection is $w_n = 0.05L$.

Declaration of interests

☒ The authors declare that they have no known competing financial interests or personal relationships that could have appeared to influence the work reported in this paper.

☐The authors declare the following financial interests/personal relationships which may be considered as potential competing interests: